Temperature dependence of electron-phonon interactions in vanadium

F. C. Yang, O. Hellman, and B. Fultz

Phys. Rev. B **101**, 094305 — Published 12 March 2020

DOI: 10.1103/PhysRevB.101.094305

The Temperature Dependence of Electron-Phonon Interactions in Vanadium

F. C. Yang,[1] O. Hellman,[1] and B. Fultz[1]

[1] *Applied Physics and Materials Science, California Institute of Technology, Pasadena, CA 91125*

(Dated: January 8, 2020)

First-principles calculations were used to study the Fermi surface of body-centered cubic vanadium at elevated temperatures. Supercell calculations accounted for effects of thermal atom displacements on band energies, and band unfolding was used to project the spectral weight of the electron states into the Brillouin zone of a standard bcc unit cell. An electronic topological transition (ETT, or Lifshitz transition) occurred near the Γ point with increasing temperature, but the large thermal smearings from the atomic disorder and the Fermi-Dirac distribution reduced the effect of this ETT on the electron-phonon interactions. The phonon dispersions showed thermal stiffening of their Kohn anomalies near the Γ point, and of the longitudinal N phonon mode. In general the effects of the ETT were overcome by the thermal smearing of the Fermi surface that reduces the spanning vector densities for anomalous phonon modes.

I. INTRODUCTION

Vanadium is a body-centered cubic (bcc) metal with some of the strongest electron-phonon coupling for a pure element [1]. It is a superconductor with a transition temperature $T_c = 5.3$ K, one of the highest of the elemental superconductors [2]. Experimental and computational studies on the superconductive, electronic, and mechanical properties of vanadium at high pressures have revealed anomalies in the elastic constants and a positive relationship between the superconducting transition temperature with pressure [3–6].

Elemental vanadium also displays anomalous behavior with temperature. The temperature dependence of the elastic constant C_{44} has two points of inflection at approximately 800 K and 1600 K [7]. Inelastic neutron scattering (INS) experiments have shown that the increase in the vibrational entropy of vanadium from thermal expansion is cancelled by nonharmonic thermal stiffening [8] attributed to an adiabatic electron-phonon interaction (EPI) broadening of the sharp features in the electronic density of states (DOS). The strength of the EPI was related to the decrease in the electronic DOS at the Fermi level [9].

Electron-phonon interactions at low temperatures have been extensively studied for almost a century. Advances over the past two decades have allowed us to calculate materials properties related to these electron-phonon interactions from first-principles [10]. These state-of-the-art methods for calculating properties from the EPI are based on density functional perturbation theory (DFPT) [11], which does not adequately describe thermal effects observed at finite temperatures, such as anharmonic lattice dynamics. The adiabatic EPI at high temperatures had been best understood by studying the changes in the average phonon energies and the electronic DOS [9, 12, 13]. We are only now starting to see advances in first-principles computational methods for studying finite temperature electron-phonon interactions [14].

In a recent study of the adiabatic EPI, the thermal phonon softening in FeTi was linked to the appearance of new features on the Fermi surface with temperature [15]. The adiabatic EPI was altered dramatically by a thermally-driven electronic topological transition (ETT), a novel Lifshitz transition [16] that had been rarely observed with temperature [17]. It was suggested that a thermally-driven ETT may be observed in other materials with occupied or unoccupied electronic bands that are a few $k_B T$ from the Fermi level at low temperatures [15].

It was reported that the adiabatic EPI in vanadium saturates at high temperatures owing to the complete smearing of a peak in the electronic DOS at the Fermi level [9, 12, 13]. This correlated well with the softening of phonons past 1000 K. In this present work, we study the nonlinear nature of the phonon frequency shifts from the adiabatic EPI and investigate if this behavior can be attributed to a thermally-driven ETT using computational methods that have evolved from the methods employed in the study of FeTi [15].

We report changes in the Fermi surface of bcc V with temperature, finding new features with temperature, but a large broadening in energy of the Fermi surface. The broadening originates from effects of comparable magnitude from the displacements of atoms owing to the occupancy of phonon modes, and from the distribution of electron occupancies by the Fermi-Dirac distribution. Electron-phonon interactions were assessed by how a phonon could couple an occupied electron state to an unoccupied state, but with thermal broadening the occupied state was sometimes below the energy of the unoccupied state. Although temperature induced an electronic topological transition in the Fermi surface (a Lifshitz transition) near the Γ point, this ETT had less of an effect on the EPI than did the thermal broadening of the Fermi surface.

II. COMPUTATION

A. Phonon Calculations

Phonon frequencies at elevated temperatures were calculated with a modified temperature dependent effective potential (TDEP) method [18–20]. In the TDEP procedure, the Born-Oppenheimer surface of a material at a given temperature is sampled with *ab initio* molecular dynamics (AIMD). The energies, displacements, and forces on thermally displaced atoms are recorded over time. With these energy-force-displacement data sets, force constants are obtained with a least-squares fit of a model Hamiltonian to the potential-energy surface:

$$\mathcal{H} = U_0 + \sum_i \frac{\mathbf{p}_i^2}{2m_i} + \frac{1}{2!}\sum_{ij\alpha\beta} \Phi_{ij}^{\alpha\beta} u_i^\alpha u_j^\beta + \frac{1}{3!}\sum_{ijk\alpha\beta\gamma} \Phi_{ijk}^{\alpha\beta\gamma} u_i^\alpha u_j^\beta u_k^\gamma, \tag{1}$$

where $\mathbf{p}_i$ and u_i are the momentum and displacement of atom i, respectively, and $\alpha\beta\gamma$ are Cartesian components. The temperature-dependent U_0 is a fit parameter for the baseline of the potential energy surface [19]. The quadratic force constants Φ_{ij} capture temperature-dependent nonharmonic effects and are used to calculate phonon frequencies ω shifted by these effects [19]. These quadratic force constants are also renormalized by the quartic term in the potential [21, 22]. The cubic force constants Φ_{ijk} capture phonon-phonon interactions (PPI) that contribute to the broadening and additional shifts of phonon modes.

The same model Hamiltonian was used in this work, except the Born-Oppenheimer surface was sampled by multiple density functional theory (DFT) calculations on supercells of thermally displaced atoms generated by stochastic sampling of a canonical ensemble. For a cell of N_a atoms with mass m_i, a harmonic normal-mode transformation was used to generate positions $\{u_i\}$ consistent with a canonical ensemble:

$$u_i = \sum_{s=1}^{3N_a} \epsilon_{is} \langle A_{is} \rangle \sqrt{-2\ln\xi_1} \sin(2\pi\xi_2), \tag{2}$$

where ξ_n are uniformly distributed numbers between 0 and 1 producing the Box-Muller transform. $\langle A_{is} \rangle$ is the thermal amplitude of the normal mode s with eigenvector ϵ_{is} and frequency ω_s [23, 24]:

$$\langle A_{is} \rangle = \underbrace{\frac{1}{\omega_s}\sqrt{\frac{\hbar\omega_s(n_s+\frac{1}{2})}{m_i}}}_{\text{quantum}} \approx \underbrace{\frac{1}{\omega_s}\sqrt{\frac{k_\mathrm{B}T}{m_i}}}_{\text{classical}}, \tag{3}$$

where $n_s = (e^{\hbar\omega_s/k_\mathrm{B}T} - 1)^{-1}$ is the thermal occupation of mode s, and $\hbar\omega \ll k_\mathrm{B}T$ denotes the classical limit at high temperatures.

These stochastically generated thermal displacements from Eqs. 2 and 3 sample the Born-Oppenheimer surface in the stochastically-initialized temperature-dependent effective potential (s-TDEP) method [18–20, 25, 26]. This method approximates the inclusion of zero-point motion not included in AIMD simulations and connects seamlessly to the classical limit at high temperature. The s-TDEP procedure can be used to calculate force constants capturing anomalous high-temperature effects [25–28] to low-temperature quantum effects [29, 30] at a much lower computational cost than what is required by AIMD. The force constants calculated with this method are numerically converged with respect to the number of configurations and supercell size. The convergence of the force constants and the baseline U_0 was further ensured by repeating DFT calculations on new snapshots generated from force constants from the previous iteration of s-TDEP. The force constants used to generate the supercells in the first iteration of s-TDEP were generated through a model pair potential as described in Ref. [25]. The weakness of the s-TDEP method is that it relies on Gaussian distributions of coordinates generated by Eq. 2.

The *ab initio* DFT calculations were performed with the projector augmented wave [31] formalism as implemented in VASP [32, 33]. All calculations used a supercell with 250 vanadium atoms, a $3 \times 3 \times 3$ Monkhorst-Pack [34] k-point grid, and a plane-wave energy cutoff of 580 eV. The exchange-correlation energy was calculated with the PBE functional [35].

These force constants were calculated on a grid of six temperatures, $\{0, 300, 550, 750, 1250, 1650\}$ K, and six volumes. The quadratic and cubic interatomic force constants for temperatures and volumes between these grid points were obtained by interpolation. Through three iterations of the s-TDEP procedure, we obtained the Helmholtz free energy surface $F(V,T)$:

$$F(V,T) = U_0(V,T) + F_\mathrm{vib}(V,T). \tag{4}$$

$U_0(V,T)$ is the baseline from Eq. 1. $F_\mathrm{vib}(V,T)$ is from lattice vibrations:

$$F_\mathrm{vib} = \int_0^\infty g(\omega) \left\{ k_\mathrm{B}T \ln\left[1 - \exp\left(-\frac{\hbar\omega}{k_\mathrm{B}T}\right)\right] + \frac{\hbar\omega}{2} \right\} \mathrm{d}\omega, \tag{5}$$

where $g(\omega)$ is the phonon density of states calculated from the phonons in the first Brillouin zone,

$$g(\omega) = \sum_s \delta(\omega - \omega_s). \tag{6}$$

The electronic entropy, obtained from the DFT calculations, made a small contribution to U_0 of Eq. 1. We minimized the free energy to calculate the equilibrium volume at each temperature and evaluated the phonon frequencies at these conditions.

We then corrected our phonon frequencies by calculating the linewidths Γ_s and shifts Δ_s arising from anharmonicity, or phonon-phonon interactions. This required the many-body perturbation calculation of the real and imaginary parts of the phonon self-energy

$\Sigma(\Omega) = \Delta(\Omega) + \mathrm{i}\Gamma(\Omega)$, where $E = \hbar\Omega$ is a probing energy [36, 37]. The imaginary component $\Gamma(\Omega)$ is

$$\Gamma_s(\Omega) = \frac{\hbar\pi}{16} \sum_{s's''} \left|\Phi_{ss's''}\right|^2 \{(n_{s'} + n_{s''} + 1)\delta(\Omega - \omega_{s'} - \omega_{s''}) + (n_{s'} - n_{s''})\left[\delta(\Omega - \omega_{s'} + \omega_{s''}) - \delta(\Omega + \omega_{s'} - \omega_{s''})\right]\} \tag{7}$$

and the real component is obtained by a Kramers-Kronig transformation

$$\Delta(\Omega) = \frac{1}{\pi} \int \frac{\Gamma(\omega)}{\omega - \Omega} \mathrm{d}\omega. \tag{8}$$

The imaginary component of the self-energy is a sum over all possible three-phonon interactions, where $\Phi_{ss's''}$ is the three-phonon matrix element determined from the cubic force constants Φ_{ijk}. The $\Gamma(\Omega)$ and $\Delta(\Omega)$ were calculated with a $28 \times 28 \times 28$ q-grid.

Anharmonic phonon DOS curves were calculated with the real and imaginary parts of the phonon self-energy:

$$g_{\mathrm{anh}}(\omega) = \sum_s \frac{2\omega_s \Gamma_s(\omega)}{\left[\omega^2 - \omega_s^2 - 2\omega_s \Delta_s(\omega)\right]^2 + 4\omega_s^2 \Gamma_s^2(\omega)}. \tag{9}$$

If both Δ and Γ go to zero, Eq. 9 reduces to Eq. 6.

Calculations were also performed with the quasiharmonic (QH) approximation, which gave a contribution of thermal expansion to phonon frequencies without the anharmonic corrections of Eqs. 7 and 8. These QH calculations were performed by interpolating the 0 K quadratic force constants to volumes obtained from the minimization of the QH free energy.

B. Electronic Band Unfolding

The electronic band structure of vanadium at 0 K is usually obtained from a DFT calculation on a static lattice using a primitive unit cell (PC). We model finite temperatures with calculations on supercells (SC) containing thermally-displaced atoms. The electronic bands from these calculations are folded into a smaller SC Brillouin zone (SCBZ), giving rise to complicated band structures that cannot be directly compared to 0 K electronic bands in the larger primitive cell Brillouin zone (PCBZ).

We can recover an approximation of these supercell electronic bands in the PCBZ through band unfolding [38] as implemented with the BANDUP software package [39, 40]. In brief, BANDUP gives the spectral function $A(\mathbf{k}; \varepsilon)$ from supercell calculations [38, 41]

$$\begin{aligned} A(\mathbf{k}, \varepsilon) &= \sum_m P_{m\mathbf{K}}(\mathbf{k}) \delta(\varepsilon - \varepsilon_m(\mathbf{K})) \\ &= \sum_m \sum_n \left|\langle m\mathbf{K} | n\mathbf{k}\rangle\right|^2 \delta(\varepsilon - \varepsilon_m(\mathbf{K})), \end{aligned} \tag{10}$$

where $\mathbf{k}$ and $|n\mathbf{k}\rangle$ are electron wavevectors and eigenstates in the PCBZ, and $\mathbf{K}$ and $|m\mathbf{K}\rangle$ are electron wavevectors and eigenstates in the SCBZ. The spectral weight $P_{m\mathbf{K}}(\mathbf{k})$ is the projection of $|m\mathbf{K}\rangle$ on all of the PC Bloch states $|n\mathbf{k}\rangle$ at the PC wavevector $\mathbf{k}$. The only pairs of wavevectors ($\mathbf{k}$, $\mathbf{K}$) that are included in the sum in Eq. 10 are those in which $\mathbf{K}$ unfolds onto $\mathbf{k}$:

$$\mathbf{k} = \mathbf{K} + \mathbf{G}, \tag{11}$$

where $\mathbf{G}$ is a reciprocal lattice vector in the SBCZ.

The unfolded electronic band structure is represented as an effective PC band structure (EBS). In BANDUP, this quantity is calculated from the spectral function with the infinitesimal version of the cumulative probability function $S_{\mathbf{k}}(\varepsilon)$. The quantity $\mathrm{d}S_{\mathbf{k}}(\varepsilon) = A(\mathbf{k}, \varepsilon)\mathrm{d}\varepsilon$ represents the number of PC electronic bands at the PC wavevector $\mathbf{k}$ crossing the energy interval $(\varepsilon, \varepsilon + \mathrm{d}\varepsilon)$. We can obtain the EBS $\delta N(\mathbf{k}_i, \varepsilon_j)$ in a region of interest in the $(\mathbf{k}, \varepsilon)$ space with energy intervals of size $\delta\varepsilon$:

$$\begin{aligned} \delta N(\mathbf{k}_i, \varepsilon_j) &= \int_{\varepsilon_j - \delta\varepsilon/2}^{\varepsilon_j + \delta\varepsilon/2} \mathrm{d}S_{\mathbf{k}_i}(\varepsilon) \\ &= \sum_m P_{m\mathbf{K}}(\mathbf{k}_i) \int_{\varepsilon_j - \delta\varepsilon/2}^{\varepsilon_j + \delta\varepsilon/2} \delta(\varepsilon - \varepsilon_m(\mathbf{K})) \mathrm{d}\varepsilon \end{aligned} \tag{12}$$

The EBS gives the number of PC electronic bands crossing $(\mathbf{k}_i, \varepsilon_j)$.

The EBS calculated from this unfolding procedure is exactly equal to the PC electronic band structure only for perfect supercells, where the static atoms are on their crystallographic sites. The EBS calculated with BANDUP shows the effects of perturbations on the electronic structure such as from crystallographic defects and atom substitutions [39, 40].

For the electronic band structure at 1100 K, we assembled an ensemble of supercells $\{\eta\}$ with thermal displacements $\{u_i\}$ generated with Eqs. 2 and 3 and phonon frequencies at 1100 K. For each of the configurations η with displacements $\{u_i\}$, we calculated the EBS $\delta N_\eta(\mathbf{k}_i, \varepsilon_j)$, where $\varepsilon_j \equiv E_j - E_{\mathrm{F}}^{(\eta)}$ is defined with respect to the Fermi energy $E_{\mathrm{F}}^{(\eta)}$ calculated for the supercell η. The thermal atomic displacements from their crystallographic sites are treated as perturbations. Our calculated electronic structure at 1100 K is the ensemble average of the EBS $\langle \delta N_\eta \rangle$. This methodology was previously used to model finite temperature electronic bands in FeTi [15].

C. Density Functional Perturbation Theory

Density functional perturbation theory calculations [11] were performed with Quantum ESPRESSO [42, 43] with ultrasoft pseudopotentials [44] and the Perdew-Burke-Ernzerhof (PBE) exchange-correlation functional [35]. The electron-phonon interaction matrix elements were first calculated on a $72 \times 72 \times 72$ k-point mesh and a $12 \times 12 \times 12$ q-point mesh, and later interpolated to 720 q-points along the high symmetry lines in the bcc Brillouin zone through Fourier interpolation implemented in

Quantum ESPRESSO. The matrix elements were then used to compute the scattering rates of phonons by electrons:

$$\frac{1}{\tau_{\mathbf{q}\nu}} = \frac{2\pi}{\hbar}\sum_{mn}\int \frac{\mathrm{d}\mathbf{k}}{\Omega_{\mathrm{BZ}}}|g^{\nu}_{mn}(\mathbf{k},\mathbf{q})|^2\,(f_{n\mathbf{k}} - f_{m\mathbf{k}+\mathbf{q}}) \times \delta(\varepsilon_m(\mathbf{k}+\mathbf{q}) - \varepsilon_n(\mathbf{k}) - \hbar\omega_{\mathbf{q}\nu}), \quad (13)$$

where $g^{\nu}_{mn}(\mathbf{k},\mathbf{q})$ is the electron-phonon interaction matrix element associated with a phonon mode ν with wavevector $\mathbf{q}$ and two electronic states with the eigenstates $|m\mathbf{k}\rangle$ and $|n\mathbf{k}+\mathbf{q}\rangle$, and $f_{m\mathbf{k}}$ is the Fermi-Dirac distribution for electrons. The electron-phonon coupling strength associated with this interaction is:

$$\lambda_{\mathbf{q}\nu} = \frac{1/\tau_{\mathbf{q}\nu}}{\pi N(E_{\mathrm{F}})\omega_{\mathbf{q}\nu}} \quad (14)$$

where $N(E_{\mathrm{F}})$ is the electronic DOS at the Fermi level.

III. RESULTS

A. Phonons

Figure 1(b) shows phonon densities of states of vanadium calculated with the s-TDEP method at temperatures from 0 to 1650 K. There is no significant broadening from PPI. The high-energy longitudinal phonon modes from 26 to 30 meV stiffen before they begin to slowly soften with temperature. This anomalous behavior is seen more clearly in the plot of average phonon energies derived from the phonon DOS in Fig. 1(c):

$$\langle E\rangle = \int E \times g(E)dE \quad (15)$$

The average phonon energy increases with temperature to approximately 750 K, and then begins to decrease. This behavior strongly deviates from what is predicted by the QH model, where the average phonon energy decreases in the entire temperature range as the crystal expands. The calculated average phonon energies and their thermal trend are in good agreement with inelastic neutron scattering (INS) measurements of the vanadium phonon DOS [8, 9, 45].

Our calculated spectral function $S(\mathbf{q},\omega)$ is compared to phonon dispersions measured with thermal diffuse x-ray scattering (TDS) [46] and inelastic x-ray scattering (IXS) [47] in Fig. 2. The agreement is good. The s-TDEP spectral function agrees with both the IXS (particularly along the H-P and Γ-P directions) and the TDS measurements (the longitudinal branch along the Γ-H and Γ-N directions). The Kohn anomalies [48] are more pronounced in the s-TDEP spectral function along Γ-H and Γ-N than the TDS and IXS measurements, and there is some disrepancy for the transverse acoustic TA_1 phonon mode at the N symmetry point. There is a crossover of the longitudinal phonon branch with the the

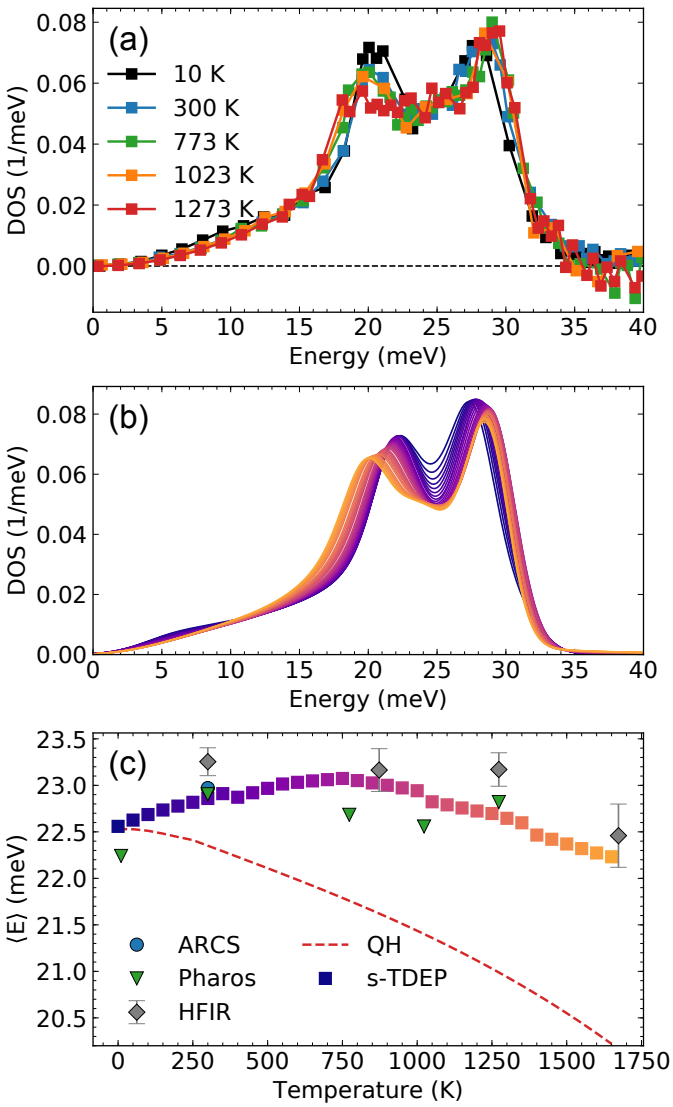

FIG. 1. (a) Phonon DOS curves from experimental measurements on the PHAROS spectrometer from 10 - 1273 K [9]. (b) The phonon DOS curves of vanadium calculated with the s-TDEP method at temperatures from 0 (dark purple) to 1650 K (orange). (c) Average phonon energies of vanadium calculated with the s-TDEP method (identical colors to those shown in (b)), shown together with average phonon energies from inelastic neutron scattering measurements (Refs. [8, 9, 45]). The dashed red curve corresponds to quasiharmonic (QH) behavior as calculated from first-principles.

TA_2 branch at the N symmetry point in all phonon dispersions. This anomaly and many other features seen in our s-TDEP spectral function were observed in the phonon dispersions calculated with DFPT by Luo *et al.* [4].

From 0 to 1650 K (Fig. 3), many phonon modes soften with temperature, including the transverse acoustic modes at the N symmetry point and the phonon modes at the H and P symmetry points. A few phonon modes stiffen before they begin softening with tempera-

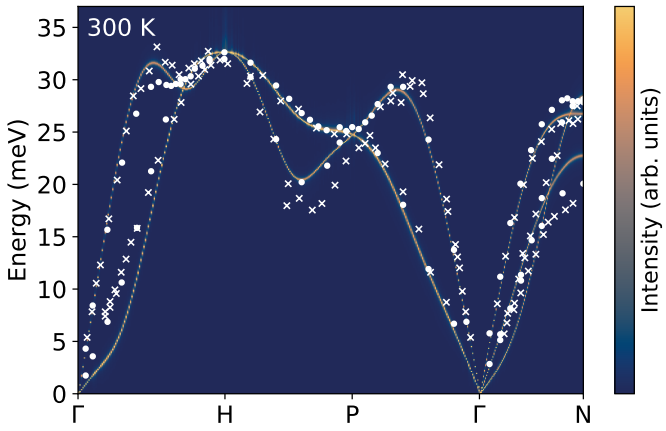

FIG. 2. The 300 K spectral function calculated with s-TDEP along the high-symmetry directions, plotted together with measurements from thermal diffuse x-ray scattering (crosses) [46] and inelastic x-ray scattering (dots) [47].

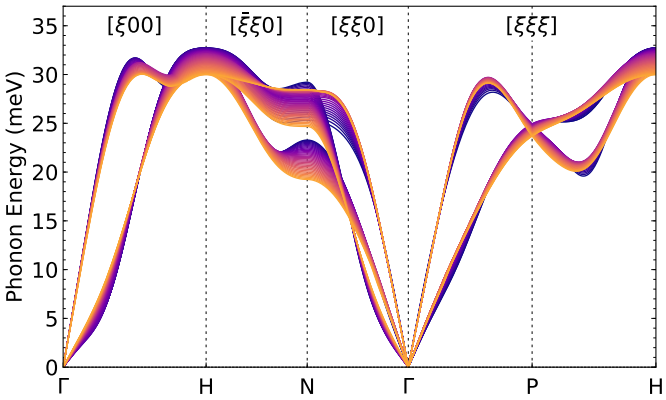

FIG. 3. Phonon dispersion curves of vanadium calculated with the s-TDEP method at temperatures from 0 (dark purple) to 1650 K (orange). Vector coordinates are written in simple cubic lattice coordinates.

ture, such as the longitudinal phonon mode at $\mathbf{q} = \left[\frac{1}{3}\frac{1}{3}\frac{1}{3}\right]$ along the Γ-P direction. A number of phonon modes stiffen with temperature, including the Kohn anomalies close to the Γ point along the Γ-H, Γ-N, and Γ-P directions. The anomalous crossover of the longitudinal and TA_2 phonon modes at the N symmetry point is no longer present at high temperatures because the longitudinal phonon mode stiffens strongly with temperature. The stiffening of the longitudinal phonon modes at the N symmetry point and $\mathbf{q} = \left[\frac{1}{3}\frac{1}{3}\frac{1}{3}\right]$ contribute to the anomalous behavior of the longitudinal peak in the phonon DOS.

B. Electronic Band Structure

Figure 4 shows the electronic band structure of vanadium at 1100 K calculated with band unfolding implemented in BANDUP. The 1100 K electronic band structure is the average of the EBS $\langle \delta N_\eta \rangle$ calculated from 15 stochastically generated supercells with thermal displacements characteristic of 1100 K. Each EBS was calculated from –1 to 1 eV along the high-symmetry directions of the bcc Brillouin zone in $(\mathbf{k}, \varepsilon)$ space.

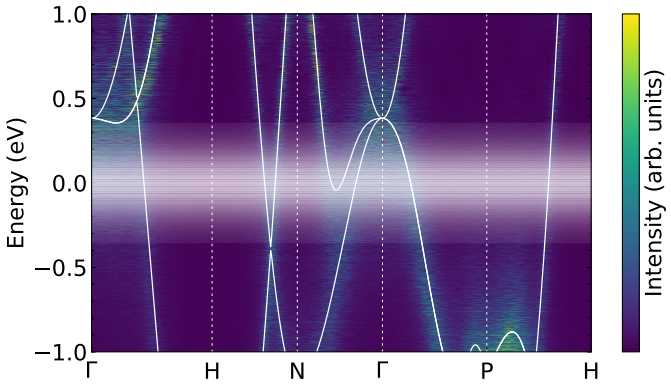

FIG. 4. Unfolded electronic bands at 1100 K, compared with 0 K electronic bands in white. The Fermi level is represented as a spread in energies.

The Fermi level at 1100 K is represented as a distribution of energies. This accounts for how the occupation of electronic states is neither exactly 0 nor exactly 1 within a few $k_B T$ around the Fermi energy, as specified by the Fermi-Dirac distribution at finite temperature. This is our visual representation of the *thermal layer* $\Delta\varepsilon$ of thickness proportional to $k_B T$ in which there are electrons together with empty states into which they may be scattered [49].

We do not observe significant shifts in the positions of the electronic bands from 0 to 1100 K. Instead there is a strong broadening of electronic bands with thermal disorder, a high temperature phenomenon that is consistent with predictions from the Allen-Heine-Cardona (AHC) theory [50–55]. Electronic states at the Γ point intersect the thermal layer because of this strong broadening.

C. Fermi Surface

We calculated the Fermi surface of vanadium at 0 and 1100 K through band unfolding implemented with BANDUP. The EBS for a given supercell η was calculated for ε from −0.50 to +0.50 eV for all of the k-points in a $50 \times 50 \times 50$ k-point grid within the bcc irreducible Brillouin zone. The Fermi surface $F(\mathbf{k}, \varepsilon)$ is our average EBS $\langle \delta N_\eta \rangle$ unfolded from the irreducible Brillouin zone to the full Brillouin zone. We unfold the EBS by applying the symmetry operations used to recover the full Brillouin zone from the irreducible Brillouin zone.

For visualization, each k-point in the Brillouin zone is assigned an intensity from integrating the average EBS

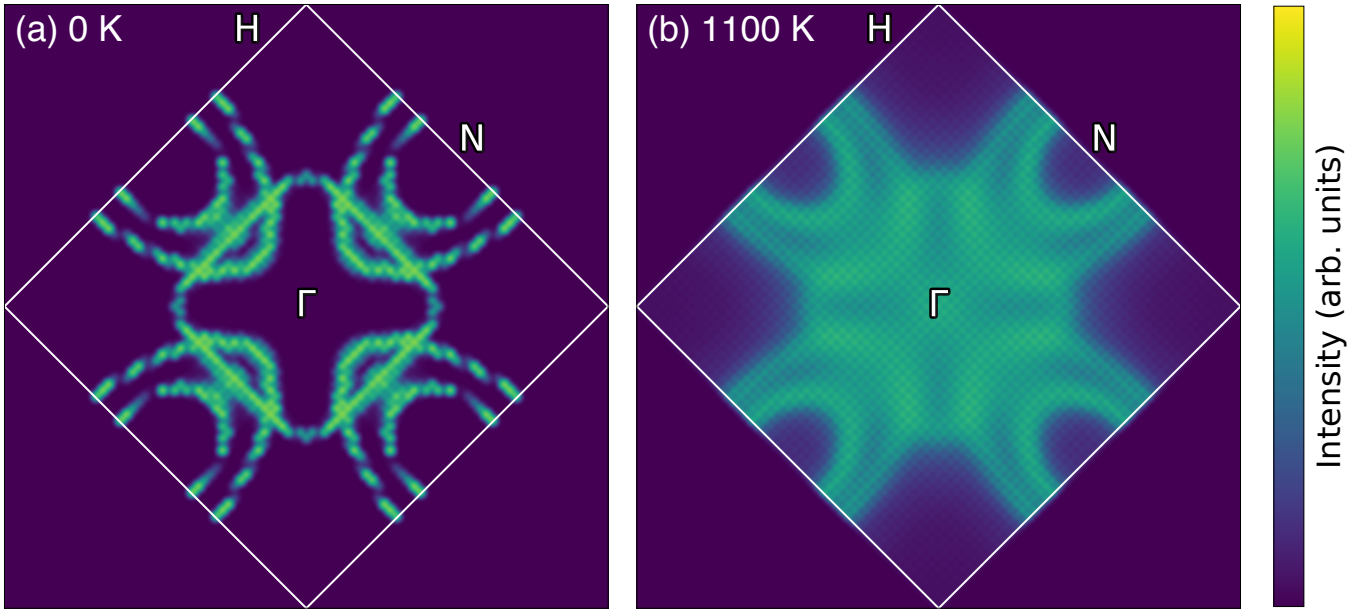

FIG. 5. The {100} cross sections of the Fermi surface of vanadium at (a) 0 K and (b) 1100 K (cross section indices are expressed in simple cubic coordinates).

$\langle \delta N_\eta \rangle$

$$I(\mathbf{k}) = \int_{\varepsilon_{\min}}^{\varepsilon_{\max}} \langle \delta N_\eta(\mathbf{k}, \varepsilon) \rangle \left(-\frac{\partial f(\varepsilon, T)}{\partial \varepsilon} \right) \mathrm{d}\varepsilon. \qquad (16)$$

The EBS is weighted against the derivative of the Fermi-Dirac distribution $f(\varepsilon, T)$ with respect to energy. This provides a distribution function with a width proportional to the thermal layer [49], which was represented as the distribution of energies $\Delta\varepsilon$ around the Fermi energy in Fig. 4. For 0 K, this distribution function is a Dirac delta function, yielding intensities expected from the definition of the 0 K Fermi surface as the map of k-points where electronic bands intersect the Fermi energy ($\varepsilon = E - E_\mathrm{F} = 0$).

The {100} cross sections of the Fermi surface are shown in Fig. 5 for 0 and 1100 K. The cross section of the 0 K Fermi surface in Fig. 5(a) is in excellent agreement with that calculated by Landa, *et al*. [6]. The broadening Δk of the electronic states in Fig. 5(b) arises from both thermal atomic displacements and the thermal layer. Representing the finite temperature Fermi surface as an overlay of surfaces defined in the thermal layer allows us to account for all of the electronic states relevant for thermodynamic and transport properties, such as the electronic specific heat and conductivity [49].

The values for the intensity $I(\mathbf{k})$ of the 1100 K Fermi surface are lower than the values for the 0 K Fermi surface. The broadening Δk of the Fermi surface washes away sharp features of the 0 K Fermi surface, especially for the closed distorted hole-ellipsoids centered at the N symmetry points. The distorted octahedron closed hole-pocket centered at the Γ point at 0 K is no longer distinguishable from these hole-ellipsoids at elevated temperatures. We observe a number of additional electronic states at the Γ point at 1100 K arising from the broadening of the triply degenerate electronic band seen in Fig. 4. The formerly hollow octahedron is filled up with these new electronic states in a thermally-driven ETT.

IV. DISCUSSION

A. Fermi Surface Nesting

The 0 K electron-phonon coupling strength $\lambda_{\mathbf{q}\nu}$ was calculated for vanadium and is plotted in Fig. 6. The maximum value for the electron-phonon coupling strength is observed for the transverse phonon branch near the Γ point along the Γ-H direction, coinciding with the Kohn anomaly [48]. Peaks in the electron-phonon coupling strength are also observed for transverse phonon branches close to the Γ point along the Γ-N and Γ-P directions. A high value for the electron-phonon coupling strength is observed for the longitudinal phonon mode at the N point. This is the same phonon mode that crosses over with the high transverse acoustic mode. All of these phonon modes stiffen with temperature (Fig. 3).

The peak in the electron-phonon coupling strength along the Γ-H direction coincides with the peak in the generalized susceptibility found by Landa, *et al* at the wavevector $\mathbf{q} = [0.24, 0, 0]$ [6]. The wavevector $\mathbf{q} = [0.24, 0, 0]$ spans nesting features, pairs of parallel sheets in the Fermi surface $\{|n\mathbf{k}\rangle\}$ and $\{|m\mathbf{k}'\rangle\}$ that are related by $\mathbf{k}' = \mathbf{k} + \mathbf{q} + \mathbf{g}$, where $\mathbf{g}$ is a reciprocal lattice vector. A high density of these *spanning vectors* results in high numbers of nonzero terms in Eq. 13. The peaks in

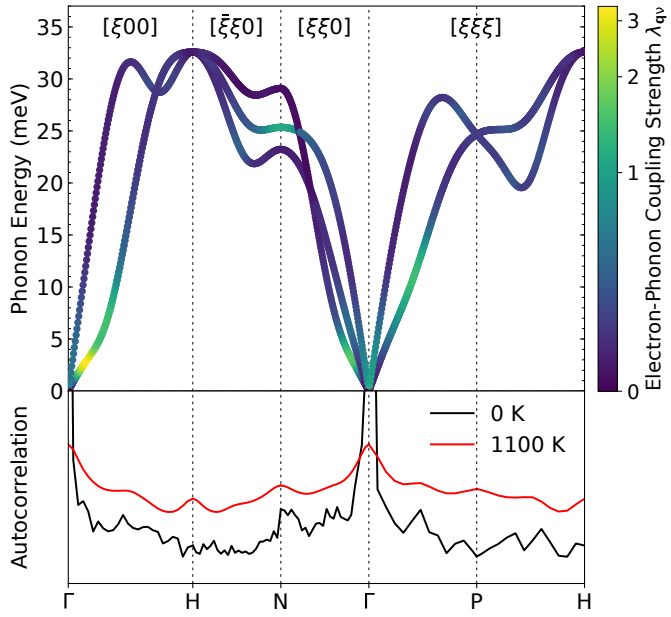

FIG. 6. (Top) 0 K electron-phonon coupling strengths of phonon modes calculated with Quantum ESPRESSO displayed over the 0 K vanadium phonon dispersion calculated with s-TDEP. (Bottom) Autocorrelation of the Fermi surface at 0 and 1100 K.

the electron-phonon coupling strength along Γ-N, Γ-P, and at N may correspond to additional wavevectors that span Fermi surface nesting features.

We can probe for spanning wavevectors by calculating the periodic autocorrelation of the Fermi surface

$$R(\mathbf{q}) = \frac{1}{N_{\text{Fermi}}} \sum_{\mathbf{k}} I(\mathbf{k}) I(\mathbf{k}+\mathbf{q}+\mathbf{g}), \tag{17}$$

where $I(\mathbf{k})$ is the integrated Fermi surface intensity calculated from Eq. 16 and N_{Fermi} is the number of k-points on the Fermi surface. We expect peaks in the autocorrelation where nesting features in $I(\mathbf{k})$ and $I(\mathbf{k}+\mathbf{q}+\mathbf{g})$ overlap.

The autocorrelations of the 0 and 1100 K Fermi surfaces are plotted in the bottom panel of Fig. 6. A sharp peak is observed in the 0 K autocorrelation at $\mathbf{q} = [0.24, 0, 0]$ along the Γ-H direction, approximately lining up with the location of the peak in the electron-phonon coupling strength $\lambda_{\mathbf{q}\nu}$. Similar sharp peaks are observed near the Γ point along the Γ-N and Γ-P directions and at the N symmetry point, approximately lining up with the peaks in $\lambda_{\mathbf{q}\nu}$.

We still observe a peak at the N symmetry point in the 1100 K Fermi surface autocorrelation. We see an additional peak at the H symmetry point. No peak is observed at $\mathbf{q} = [0.24, 0, 0]$. None of the peaks in the 1100 K autocorrelation are as narrow as the 0 K peaks, and the peaks barely stand out from the baseline. The broad peaks in the 1100 K autocorrelation indicate that electron-phonon interactions are reduced as nesting features are smeared out with the thermal broadening observed in Fig. 5.

B. Temperature Dependence of Electron-Phonon Interactions

We can get a closer look at how changes in the Fermi surface with temperature affect electron-phonon interactions by calculating the density of specific spanning vectors $D_\nu(\mathbf{q})$ at 0 and 1100 K. By comparing the spanning vector densities of phonon modes between the two temperatures, we can see if the number of available electron-phonon interactions are increased or decreased with temperature. We can also see if the spanning vector densities and electron-phonon interactions are impacted by the thermally-driven ETT observed in Fig. 5. We define:

$$D_\nu(\mathbf{q}) = \frac{1}{N_{\text{Fermi}}} \sum_{\mathbf{k}} \sum_{\varepsilon \in \text{TL}} \sum_{\mathbf{q}_i \in S\mathbf{q}} \left[F(\mathbf{k},\varepsilon)F(\mathbf{k}+\mathbf{q}_i+\mathbf{g},\varepsilon+\hbar\omega_{\mathbf{q}\nu}) + F(\mathbf{k}+\mathbf{q}_i+\mathbf{g},\varepsilon)F(\mathbf{k},\varepsilon+\hbar\omega_{\mathbf{q}\nu})\right] \times \left[f(\varepsilon,T)(1-f(\varepsilon+\hbar\omega_{\mathbf{q}\nu},T)) + f(\varepsilon+\hbar\omega_{\mathbf{q}\nu},T)(1-f(\varepsilon,T))\right], \tag{18}$$

where $\mathbf{q}_i$ is a vector related to $\mathbf{q}$ by symmetry. We are treating the Fermi surface F as a function of both $\mathbf{k}$ and energy ε to take the conservation of energy into account. We remind the reader that the Fermi surface function F is equal to the average EBS $\langle \delta N_\eta \rangle$:

$$F(\mathbf{k},\varepsilon) = \langle \delta N_\eta(\mathbf{k},\varepsilon) \rangle \tag{19}$$

Our calculation of $D_\nu(\mathbf{q})$ sums over all possible electron-phonon scattering processes in the window from −0.50 to +0.50 eV with respect to the Fermi energy, which covers the thermal layer (TL).

In the 0 K limit, the Fermi surface function F is either a nonzero integer or zero, and the thermal layer is localized at $E = E_{\text{F}}$. At 0 K, the sum in Eq. 18 would simply be a count of the number of spanning vectors $\mathbf{q}$ on the Fermi surface. At finite temperatures, the Fermi surface function F is interpreted as the probability of the presence of an electronic state at $(\mathbf{k},\varepsilon)$ as a consequence of electronic broadening from thermal atomic displacements. According to the Fermi-Dirac distribution terms in the second bracket in Eq. 18, electrons at energies far from the Fermi surface are less likely to be involved in

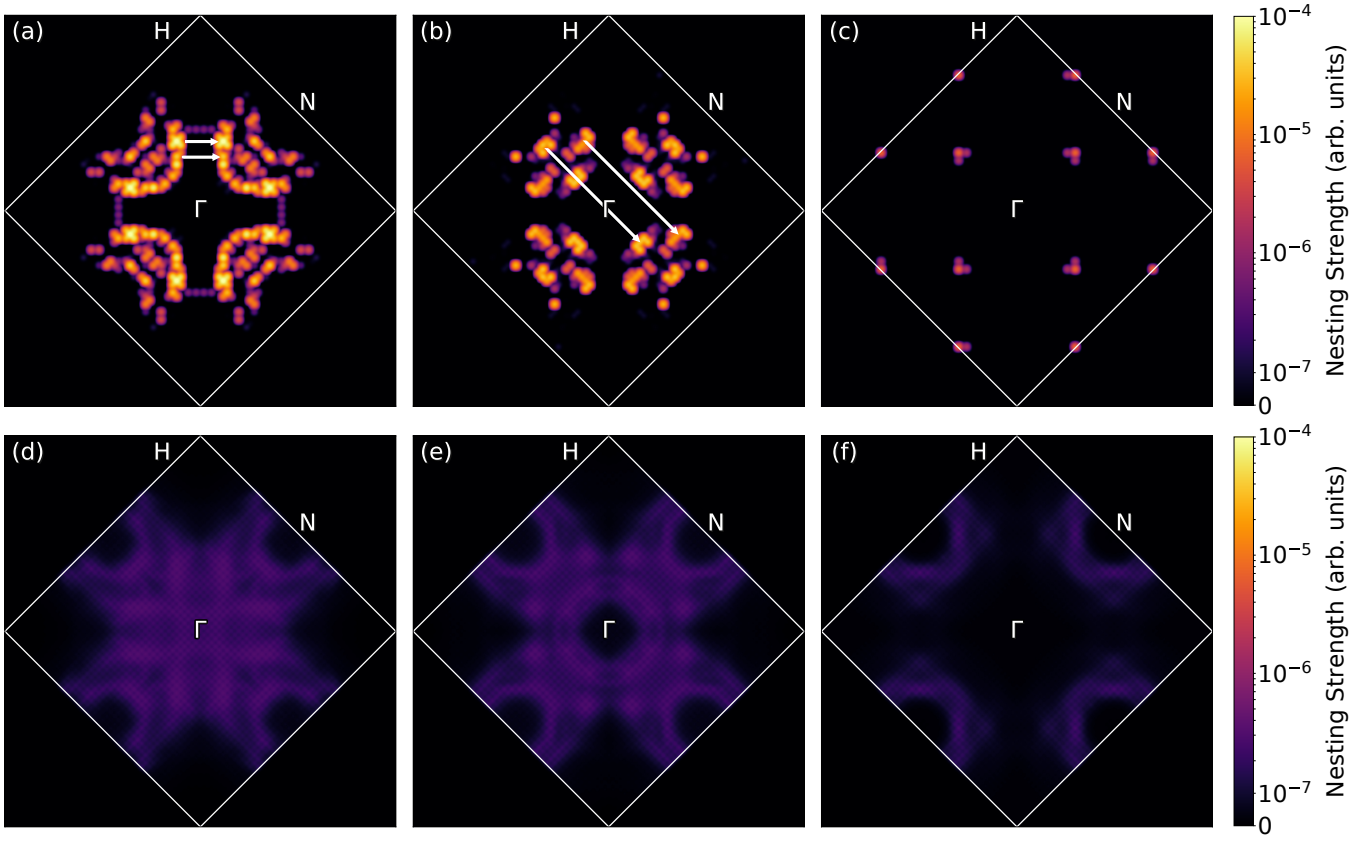

FIG. 7. (a)-(c) {100} cross sections of the 0 K Fermi surface nesting strengths for the (a) transverse phonon mode at $\mathbf{q} = [0.24, 0, 0]$, (b) the longitudinal N phonon mode, and (c) the H phonon mode. Sample $[0.24, 0, 0]$ and $[0.5, 0.5, 0]$ spanning vectors are shown in (a) and (b). (d)-(f) {100} cross sections of the 1100 K Fermi surface nesting strengths for the (d) transverse phonon mode at $\mathbf{q} = [0.24, 0, 0]$, (e) the longitudinal N phonon mode, and (f) the H phonon mode.

scattering processes due to low occupation. This is also described by the derivative of the Fermi-Dirac distribution in Eq. 16.

Information about nesting features is obtained from the summands $D_\nu^{(\mathbf{k})}(\mathbf{q})$:

$$D_\nu(\mathbf{q}) = \sum_{\mathbf{k}} D_\nu^{(\mathbf{k})}(\mathbf{q}). \tag{20}$$

The nesting strength $D_\nu^{(\mathbf{k})}(\mathbf{q})$ is the density of spanning vectors $\mathbf{q}$ for the electronic state at wavevector $\mathbf{k}$. Nesting features are composed of electronic states with high values of $D_\nu^{(\mathbf{k})}(\mathbf{q})$. Fig. 7 shows the nesting strengths $D_\nu^{(\mathbf{k})}(\mathbf{q})$ for three phonon modes: the transverse phonon mode at $\mathbf{q} = [0.24, 0, 0]$ (subfigures a and d), the longitudinal N phonon mode (subfigures b and e), and the H phonon mode (subfigures c and f).

The high 0 K electron-phonon coupling strength $\lambda_{\mathbf{q}\nu}$ for the transverse phonon mode at $\mathbf{q} = [0.24, 0, 0]$ originates with the high density of vectors spanning the flat features on the hole-ellipsoids (Fig. 7(a)). These flat features are the previously-identified nesting features associated with the Kohn anomaly along Γ-H for vanadium [6] and contribute to the high superconducting transition temperature T_c of vanadium [56, 57].

The peak in $\lambda_{\mathbf{q}\nu}$ for the longitudinal phonon mode at N is from the high density of spanning vectors between the hole-ellipsoids and the distorted octahedron (Fig. 7(b)). The crossover of the longitudinal and transverse acoustic modes at N can be attributed to the interaction of this phonon mode with these electronic states.

No notable peaks were observed in the 0 K values of $\lambda_{\mathbf{q}\nu}$ and Fermi surface autocorrelation for the H phonon mode. There are almost no nesting features for the $\mathbf{q} = [1, 0, 0]$ spanning vector (Fig. 7(c)), such that no 0 K electron-phonon interaction is observed for the H phonon mode. The vector $\mathbf{q} = [1, 0, 0]$ spans more features of the Fermi surface at 1100 K, but these features make up only a small fraction of the number of k-points making on Fermi surface at 1100 K. These features also display low nesting strengths, such that the spanning vector density $D_\nu(\mathbf{q})$ for this phonon mode is actually *reduced* by a factor of 1.73 from 0 to 1100 K. This is consistent with our observation that this phonon mode softens quasiharmonically with temperature.

The $[0.24, 0, 0]$ and $[0.5, 0.5, 0]$ vectors span more k-points in the Fermi surface at 1100 K than at 0 K, as shown in Fig. 7(d) and (e). The nesting strengths for

these phonon modes are also low. The spanning vector density for the transverse mode at $[0.24, 0, 0]$ is reduced by a factor of 2.36 from 0 to 1100 K, and the spanning vector density for the longitudinal N phonon mode is reduced by a factor of 3.09 from 0 to 1100 K.

The reduction of the spanning vector density for the transverse mode at $[0.24, 0, 0]$ is not as severe as the reduction for the longitudinal N phonon mode, owing to the introduction of additional nesting features from the thermally-driven ETT. The thermally-driven ETT does not fully counteract the reduction in the electron-phonon interaction strength for this phonon mode, however. The $[0.5, 0.5, 0]$ vector does not span any of the new electronic states at the Γ point, so the thermally-driven ETT has no impact on the thermal evolution of the longitudinal N phonon mode. This thermally-driven ETT could plausibly counteract the phonon thermal stiffening, explaining the apparent saturation of the adiabatic EPI observed by Delaire *et al* [9] and the softening of the longitudinal peak and the average phonon energies past 750 K. However, we attribute the stiffening of the longitudinal N phonon mode only to the weakening of the low-temperature EPI owing to the thermal smearing of the Fermi surface. This phonon stiffening decreases with temperature as it is opposed by softening from thermal expansion.

V. CONCLUSIONS

The nonlinear thermal stiffening of phonons in vanadium measured by inelastic neutron scattering was reproduced with first-principles calculations. The Fermi surface of vanadium was calculated at 0 K and high temperatures through band unfolding procedures. The sharp features of the Fermi surface at low temperatures were drastically smeared with temperature from atomic displacements and from the thermal excitations of electrons. The overall weakening of the electron-phonon interactions in vanadium is primarily attributed to this thermal smearing. There is a thermally-driven electronic topological transition near the Γ point, but the thermal broadening suppressed its effects on phonons. At high temperatures, the phonon stiffening from this reduction in the EPI is counteracted by phonon softening from thermal expansion.

ACKNOWLEDGMENTS

This work was supported by DOE BES under Contract No. DE-FG02-03ER46055. The calculations performed herein were made possible by resources of the National Energy Research Scientific Computing Center, a DOE Office of Science User Facility supported by the Office of Science of the U.S. Department of Energy under Contract No. DE-AC02-05CH11231.

[1] P. B. Allen, Academic Press, New York , 478 (1999).
[2] G. Grimvall, *The Electron-Phonon Interaction in Metals* (North-Holland, Amsterdam, 1981).
[3] Y. Ding, R. Ahuja, J. Shu, P. Chow, W. Luo, and H. K. Mao, Phys. Rev. Lett. **98**, 085502 (2007).
[4] W. Luo, R. Ahuja, Y. Ding, and H. K. Mao, Proc. Natl. Acad. Sci. U.S.A. **104**, 16428 (2007).
[5] M. Ishizuka, M. Iketani, and S. Endo, Phys. Rev. B **61**, R3823(R) (2000).
[6] A. Landa, J. Klepeis, P. Söderlind, I. Naumov, O. Velikokhatnyi, L. Vitos, and A. Ruban, J. Phys.: Condens. Matter **18**, 5079 (2006).
[7] E. Walker, Solid State Commun. **28**, 587 (1978).
[8] P. D. Bogdanoff, B. Fultz, J. L. Robertson, and L. Crow, Phys. Rev. B **65**, 014303 (2001).
[9] O. Delaire, M. Kresch, J. A. Muñoz, M. S. Lucas, J. Y. Y. Lin, and B. Fultz, Phys. Rev. B **77**, 214112 (2008).
[10] F. Giustino, Rev. Mod. Phys. **89**, 015003 (2017).
[11] S. Baroni, S. de Gironcoli, A. Dal Corso, and P. Giannozzi, Rev. Mod. Phys. **73**, 515 (2001).
[12] O. Delaire, M. S. Lucas, J. A. Muñoz, M. Kresch, and B. Fultz, Phys. Rev. Lett. **101**, 105504 (2008).
[13] O. Delaire, K. Marty, M. B. Stone, P. R. C. Kent, M. S. Lucas, D. L. Abernathy, D. Mandrus, and B. C. Sales, Proc. Natl. Acad. Sci. U.S.A. 108 **108**, 4725 (2011).
[14] J. J. Zhou, O. Hellman, and M. Bernardi, Phys. Rev. Lett. **121**, 226603 (2018).
[15] F. C. Yang, J. A. Muñoz, O. Hellman, L. Mauger, M. S. Lucas, S. J. Tracy, M. B. Stone, D. L. Abernathy, Y. Xiao, and B. Fultz, Phys. Rev. Lett. **117**, 076402 (2016).
[16] I. M. Lifshitz, Sov. Phys. JETP **11**, 1130 (1960).
[17] Y. Wu, N. H. Jo, M. Ochi, L. Huang, D. Mou, S. L. Bud'ko, P. C. Canfield, N. Trivedi, R. Arita, and A. Kaminski, Phys. Rev. Lett. **115**, 166602 (2015).
[18] O. Hellman, I. A. Abrikosov, and S. I. Simak, Phys. Rev. B **84**, 180301(R) (2011).
[19] O. Hellman, P. Steneteg, I. A. Abrikosov, and S. I. Simak, Phys. Rev. B **87**, 104111 (2013).
[20] O. Hellman and I. A. Abrikosov, Phys. Rev. B **88**, 144301 (2013).
[21] M. L. Klein and G. K. Horton, J. Low Temp. Phys. **9**, 151 (1972).
[22] D. J. Hooton, Edinburgh Dublin Philos. Mag. J. Sci. **46**, 422 (1955).
[23] D. West and S. K. Estreicher, Phys. Rev. Lett. **96**, 115504 (2006).
[24] I. Errea, M. Calandra, and F. Mauri, Phys. Rev. B **89**, 064302 (2014).
[25] N. Shulumba, O. Hellman, and A. J. Minnich, Phys. Rev. B **95**, 014302 (2017).

[26] F. C. Yang, O. Hellman, M. S. Lucas, H. L. Smith, C. N. Saunders, Y. Xiao, P. Chow, and B. Fultz, Phys. Rev. B **98**, 024301 (2018).
[27] H. L. Smith, Y. Shen, D. S. Kim, F. C. Yang, C. P. Adams, C. W. Li, D. L. Abernathy, M. B. Stone, and B. Fultz, Phys. Rev. Materials **2**, 103602 (2018).
[28] J. E. Herriman, O. Hellman, and B. Fultz, Phys. Rev. B **98**, 214105 (2018).
[29] D. S. Kim, O. Hellman, J. Herriman, H. L. Smith, J. Y. Y. Lin, N. Shulumba, J. L. Niedziela, C. W. Li, D. L. Abernathy, and B. Fultz, Proc. Natl. Acad. Sci. USA **115**, 1992 (2018).
[30] N. Shulumba, O. Hellman, and A. J. Minnich, Phys. Rev. Lett. **119**, 185901 (2017).
[31] P. E. Blöchl, Phys. Rev. B **50**, 17953 (1994).
[32] G. Kresse and J. Furthmüller, Phys. Rev. B **54**, 11169 (1996).
[33] G. Kresse and J. Furthmüller, Comput. Mat. Sci. **6**, 15 (1996).
[34] H. J. Monkhorst and J. D. Pack, Phys. Rev. B **13**, 5188 (1976).
[35] J. P. Perdew, K. Burke, and M. Ernzerhof, Phys. Rev. Lett **77**, 3865 (1996).
[36] A. A. Maradudin and A. E. Fein, Phys. Rev. **128**, 2589 (1962).
[37] R. A. Cowley, Rev. Prog. Phys. **31**, 123 (1968).
[38] V. Popescu and A. Zunger, Phys. Rev. B **85**, 085201 (2012).
[39] P. V. C. Medeiros, S. Stafström, and J. Björk, Phys. Rev. B **89**, 041407(R) (2014).
[40] P. V. C. Medeiros, S. S. Tsirkin, S. Stafström, and J. Björk, Phys. Rev. B **91**, 041116(R) (2015).
[41] Y. Zhang and L.-W. Wang, Phys. Rev. B **83**, 165208 (2011).
[42] P. Giannozzi *et al.*, J. Phys.: Condens. Matter **21**, 395502 (2009).
[43] P. Giannozzi *et al.*, J. Phys.: Condens. Matter **29**, 465901 (2017).
[44] D. Vanderbilt, Phys. Rev. B **41**, 7892 (1990).
[45] J. A. Muñoz, M. S. Lucas, O. Delaire, M. L. Winterrose, L. Mauger, C. W. Li, A. O. Sheets, M. B. Stone, D. L. Abernathy, Y. Xiao, P. Chow, and B. Fultz, Phys. Rev. Lett. **107**, 115501 (2011).
[46] R. Colella and B. W. Batterman, Phys. Rev. B **1**, 3913 (1970).
[47] A. Bosak, M. Hoesch, D. Antonangeli, D. L. Farber, I. Fischer, and M. Krisch, Phys. Rev. B **78**, 020301(R) (2008).
[48] W. Kohn, Phys. Rev. Lett. **2**, 393 (1959).
[49] J. M. Ziman, *Electrons and phonons* (Clarendon Press, Oxford, 1962).
[50] P. B. Allen and V. Heine, J. Phys. C **9**, 2305 (1976).
[51] P. B. Allen and M. Cardona, Phys. Rev. B **24**, 7479 (1981).
[52] P. B. Allen and M. Cardona, Phys. Rev. B **27**, 4760 (1983).
[53] G. Antonius, S. Poncé, P. Boulanger, M. Côté, and X. Gonze, Phys. Rev. Lett. **112**, 215501 (2014).
[54] G. Antonius, S. Poncé, E. Lantagne-Hurtubise, G. Auclair, X. Gonze, and M. Côté, Phys. Rev. B **92**, 085137 (2015).
[55] S. Poncé, Y. Gillet, J. L. Janssen, A. Marini, M. Verstraete, and X. Gonze, J. Chem. Phys. **143**, 102813 (2015).
[56] W. L. McMillan, Phys. Rev. **167**, 331 (1968).
[57] P. B. Allen and R. C. Dynes, Phys. Rev. B **12**, 905 (1975).
[58] See Supplemental Material, which includes Ref. [59]−[72], at [URL will be provided by the publisher] for observations on the electrical resistivity of nonmagnetic bcc transition metals and the thermal expansion of vanadium.
[59] S. D. Brorson, A. Kazeroonian, J. S. Moodera, D. W. Face, T. K. Cheng, E. P. Ippen, M. S. Dresselhaus, and G. Dresselhaus, Phys. Rev. Lett. **64**, 2172 (1990).
[60] D. A. Papaconstantopoulos, L. L. Boyer, B. M. Klein, A. R. Williams, V. L. Morruzzi, and J. F. Janak, Phys. Rev. B **15**, 4221 (1977).
[61] L. L. Boyer, D. A. Papaconstantopoulos, and B. M. Klein, Phys. Rev. B **15**, 3685 (1977).
[62] J. M. Coombes and J. P. Carbotte, Phys. Rev. B **34**, 4622 (1986).
[63] A. Al-Lehaibi, J. C. Swihart, W. H. Butler, and F. J. Pinski, Phys. Rev. B **36**, 4103 (1987).
[64] J. Zasadzinski, D. M. Burnell, E. L. Wolf, and G. B. Arnold, Phys. Rev. B **25**, 1622 (1982).
[65] R. F. Hoyt and A. C. Mota, Solid State Commun. **18**, 139 (1976).
[66] P. D. Desai, T. K. Chu, H. M. James, and C. Y. Ho, J. Phys. Chem. Ref. Data **13**, 1069 (1984).
[67] P. D. Desai, H. M. James, and C. Y. Ho, J. Phys. Chem. Ref. Data **13**, 1097 (1984).
[68] G. W. Webb, Phys. Rev. **181**, 1127 (1969).
[69] J. M. Abraham and B. Devoit, J. Less-Common Met. **29**, 311 (1972).
[70] V. E. Peletskii, Teplofiz. Vyz. Temp. **15**, 209 (1977).
[71] K. D. Maglić, N. L. Perović, G. S. Vuković, and L. P. Zeković, Int. J. Thermophys. **15**, 963 (1994).
[72] F. Güthoff, B. Hennion, C. Herzig, W. Petry, H. R. Schober, and J. Trampenau, J. Phys.: Condens. Matter **6**, 6211 (1994).